JACS
JOURNAL OF THE AMERICAN CHEMICAL SOCIETY
Article
pubs.acs.org/JACS

Pressure-Induced Phase Transformation, Reversible Amorphization, and Anomalous Visible Light Response in Organolead Bromide Perovskite

Yonggang Wang,[*,†,‡,§] Xujie Lü,[†] Wenge Yang,[*,‡,∥] Ting Wen,[§] Liuxiang Yang,[‡] Xiangting Ren,[∥] Lin Wang,[‡,∥] Zheshuai Lin,[⊥] and Yusheng Zhao[*,†]

[†]High Pressure Science and Engineering Center, University of Nevada, Las Vegas, Nevada 89154, United States

[‡]High Pressure Synergetic Consortium (HPSynC), Geophysical Laboratory, Carnegie Institution of Washington, Argonne, Illinois 60439, United States

[§]Institute of Nanostructured Functional Materials, Huanghe Science and Technology College, Zhengzhou, Henan 450006, China

[∥]Center for High Pressure Science and Technology Advanced Research (HPSTAR), Shanghai 201203, China

[⊥]Centre for Crystal Research and Development, Technical Institute of Physics and Chemistry, Chinese Academy of Sciences, Beijing 100190, China

Supporting Information

ABSTRACT: Hydrostatic pressure, as an alternative of chemical pressure to tune the crystal structure and physical properties, is a significant technique for novel function material design and fundamental research. In this article, we report the phase stability and visible light response of the organolead bromide perovskite, $CH_3NH_3PbBr_3$ ($MAPbBr_3$), under hydrostatic pressure up to 34 GPa at room temperature. Two phase transformations below 2 GPa (from $Pm\bar{3}m$ to $Im\bar{3}$, then to $Pnma$) and a reversible amorphization starting from about 2 GPa were observed, which could be attributed to the tilting of $PbBr_6$ octahedra and destroying of long-range ordering of MA cations, respectively. The visible light response of $MAPbBr_3$ to pressure was studied by in situ photoluminescence, electric resistance, photocurrent measurements and first-principle simulations. The anomalous band gap evolution during compression with red-shift followed by blue-shift is explained by the competition between compression effect and pressure-induced amorphization. Along with the amorphization process accomplished around 25 GPa, the resistance increased by 5 orders of magnitude while the system still maintains its semiconductor characteristics and considerable response to the visible light irradiation. Our results not only show that hydrostatic pressure may provide an applicable tool for the organohalide perovskites based photovoltaic device functioning as switcher or controller, but also shed light on the exploration of more amorphous organometal composites as potential light absorber.

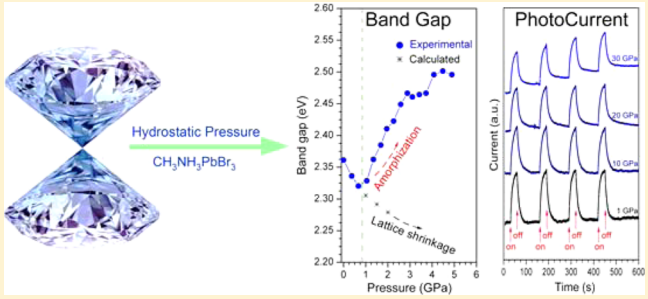

INTRODUCTION

Dye-sensitized solar cells adopting organometal halide perovskites as light absorbers have recently emerged as a promising photovoltaic technology owing to their low material cost and excellent power conversion efficiency.[1−10] Since the first report of a long-term durable solid-state perovskite solar cell by Kim et al.[11] in 2012 with a power conversion efficiency of 9.7%, the value has increased to nearly 20% in last three years.[3,12−17] The superb photovoltaic performances of organometal halides are attributed to the combination of useful properties, such as excellent charge-carrier mobility from inorganic metal-halide octahedral building blocks and their plastic mechanical properties introduced by the organic parts.

The hybrid organometal halide compounds adopt perovskite-type crystal structure with a general formula of AMX_3, in which A is an organic ammonium cation, M is Pb^{2+} or Sn^{2+} and X is typically Cl^-, Br^-, I^- or small molecular species such as BF_4^-.[18] The structure consists of a framework of corner-sharing MX_6 octahedra and organic ammonium cations in the dodecahedral A sites. Although the perovskite-type structure seems very simple, the archetypal AMX_3-type perovskites have built-in potential for complex and surprising chemical manipulations, and their optoelectronic properties can be tuned by varying the metal ions, the halide anions, the organic cation size, or by heteroelemental doping.[4,13,19−31] For instance, Seok's group[13] reported the chemical management in $CH_3NH_3Pb(I_{1-x}Br_x)_3$ for colorful, efficient and stable nanostructured solar cells. The unit cell size and band gap of the compounds were found to exhibit linear relationships with Br/I ratio, and controllable

Received: June 25, 2015
Published: August 18, 2015

DOI: 10.1021/jacs.5b06346
J. Am. Chem. Soc. 2015, 137, 11144−11149

band gaps have been achieved to cover almost the entire visible spectrum by simply changing the I/Br ratio in the composition. Kanatzidis's group[32] reported the lead-free solution-processed solid-state photovoltaic devices based on methylammonium tin iodide $CH_3NH_3SnI_3$ perovskite semiconductor as the light harvester. The replacement of lead by tin represents a step toward the low-cost and environmental friendly solar cells. They also fabricated the chemically substituted $CH_3NH_3SnI_{3-x}Br_x$ solid solutions, which exhibited controllably tuning on band gaps to cover most of the visible light spectrum. Grätzel's group[33] reported a mixed-organic-cation perovskite photovoltaics for enhanced solar light harvesting by using the mixture of formamidinium ($HN{=}CHNH_3^+$) and methylammonium ($CH_3NH_3^+$) in the A site of $APbI_3$ structure. They found this combination could lead to an enhanced short-circuit current than those based on only $CH_3NH_3^+$. These chemical modification techniques show great potential as versatile tools to tune the structural and optoelectronic properties of the light-harvesting materials toward better photovoltaic performances.

Hydrostatic pressure, as an alternative of chemical pressure that can efficiently tune the crystal structure and electronic configuration,[34−40] is a significant technique to modify the physical/chemical properties in current material science. It can not only provide insight into the structure−property relationship, but also find practical applications if the pressure is not too high for sizable material synthesis (generally <10 GPa). So far, there is no report on pressure tuning on the photovoltaic-related properties of organometal halide perovskites. There are only several pressure-related reports focused on the structure features of the materials and the applied pressure is very limited.[41,42] In this article, we report the first attempt by using hydrostatic pressure up to 38 GPa to tune the bandgap and photocurrent properties of the organolead bromide perovskite, $CH_3NH_3PbBr_3$ ($MAPbBr_3$). The crystal structure evolutions together with visible light response of $MAPbBr_3$ were studied by in situ X-ray diffraction (XRD), photoluminescence (PL), electrical resistance (ER) and photocurrent measurements. The results not only provide in-depth insight into the structure−property relationship in organometal halides, but also shed light on the future exploration of advanced photovoltaic materials.

EXPERIMENTAL DETAILS

Sample Preparation. The $MAPbBr_3$ perovskite crystals were prepared with the similar procedure reported before.[1,20,43] Briefly, CH_3NH_3Br was synthesized first by reacting 80.9 g hydrobromic acid (~40 wt %) with 31.6 g methylamine (~40 wt %) in ice bath, and stirring for 2 h. The resulting solution was then heated at 50 °C for 1 h and the colorless CH_3NH_3Br crystals formed. The CH_3NH_3Br crystals were washed three times with diethyl ether and dried under vacuum. Then equimolar quantities of freshly prepared CH_3NH_3Br (1.12 g, 10 mmol) and $PbBr_2$ (3.67 g, 10 mmol) were mixed in 50 mL *N*-dimethylformamide (DMF, ~ 40 wt %) at 60 °C with overnight stirring to produce a precursor solution. Orange crystals were obtained after treating the solution at 65 °C under vacuum for another 24 h. The products were stored in sealed glass tube for further characterizations.

In Situ High-Pressure Characterizations. A symmetrical diamond anvil cell (DAC) was employed to generate high pressure. A stainless steel gasket was preindented to 50 μm in thickness followed by laser-drilling the central part to form a 200 μm diameter hole to serve as the sample chamber. The $MAPbBr_3$ microcrystals (<1.0 mg) and a small ruby ball were loaded together in the sample chamber. No pressure-transmitting medium was used and the pressures were determined by the ruby fluorescence method.[44] The in situ high pressure angle-dispersive XRD experiments were carried out at 16 ID-B station of High-Pressure Collaborative Access Team (HPCAT) at the Advanced Phonon Source (APS), Argonne National Laboratory (ANL). A focused monochromatic X-ray beam with about 5 μm in diameter (fwhm) and wavelengths of 0.4066 Å was used for the diffraction experiments. The diffraction pattern were recorded by a two-dimensional area PILATUS detector and integrated into one-dimensional profile with the Fit2D program.[45] Structure refinements were performed by using FULLPROF program.[46]

In situ high-pressure PL spectra were measured by a Raman spectrometer with a 3 mW and 325 nm excitation laser at HPSTAR (Shanghai, China). ER was measured by a four-point-probe resistance measurement system consisting of a Keithley 6221 current source, a 2182A nanovoltmeter and 7001 voltage/current switch system. A DAC device was used to generate pressure up to 38 GPa, and a cubic boron nitride layer was inserted between the steel gasket and diamond anvil to provide electrical insulation between the electrical leads and gasket. Four gold wires were arranged to contact the sample in the chamber for resistance measurement and a quasi four-point-probe connection mode was adopted for the photocurrent measurement (see the inset photos in Figure 6). For the photocurrent measurement, an Autolab PGSTAT128N workstation was used to record the I-t data. A 20 W incandescent lamp was used as the irradiation source (~2 W/cm^2 on the sample). Because the ER changed along with the applied pressure, dark current at μA level was generated by applying a constant voltage (varies from 0.0001 to 4.0 V at a given pressure point depending on the ER. For example, 0.0001 V at 1.0 GPa and 1.0 V at 20 GPa, respectively).

First-Principles Calculations. Partial density of state (PDOS) and the pressure-bandgap relations for $MAPbBr_3$ were calculated using the plane-wave pseudopotential method based on density functional theory with CASTEP package.[47] The exchange-correlation functional is described by the local density approximation (LDA).[48] The ion-electron interactions are modeled by the ultrasoft pseudopotentials for all constituent elements, where C $2s^22p^2$, N $2s^22p^3$, Pb $6s^25d^{10}4f^{14}6P^2$ and Br $4s^23d^{10}4p^5$ electrons are treated as the valence electrons, respectively. The kinetic energy cutoff of 380 eV and Monkhorst−Pack *k*-point meshes spanning less than 0.04/Å^3 in the Brillouin zone are chosen. The starting structure models were obtained from Inorganic Crystal Structure Database (ICSD #158306). The cell parameters and atomic positions in unit cell of $MAPbBr_3$ under hydrostatic pressures varied from 0 to 2 GPa (with the interval of 0.5 GPa) are fully optimized using the quasi-Newton method.[49] The convergence thresholds between optimization cycles for energy change, maximum force, maximum stress, and maximum displacement are set as 5.0×10^{-6} eV per atom, 0.01 eV per Å, 0.02 GPa, and 5.0×10^{-4} Å, respectively. The optimization terminates when all of these criteria are satisfied. All these computational parameters have been tested to ensure the sufficient accuracy for the present purposes.

RESULTS AND DISCUSSION

At ambient conditions, $MAPbBr_3$ crystallizes in cubic perovskite-type structure consisting of corner-sharing $PbBr_6$ octahedra and organic cations located in the A sites.[41] The as-grown orange microcrystals show good phase purity in cubic phase with space group $Pm\bar{3}m$ (lattice constants of a = 8.4413(6) Å), and green emission under UV irradiation (As shown in Figure S1, S2). The sample was loaded in a symmetrical DAC for in situ high-pressure study (see the Experimental Details). Synchrotron XRD patterns of $MAPbBr_3$ were collected at different pressures during compression up to 34.0 GPa and decompression. Figure 1a shows the two-dimensional raw XRD images at four selected pressures during compression. With the increase of pressure, some sharp rings become weaker and new broad rings appear, indicating the onset of structural disorder and partial amorphization. When the applied pressure exceeds 12.5 GPa, almost all of the initial diffraction rings disappear and only four broad rings (1 strong, 3 weak) remain which can be

DOI: 10.1021/jacs.5b06346
J. Am. Chem. Soc. 2015, 137, 11144−11149

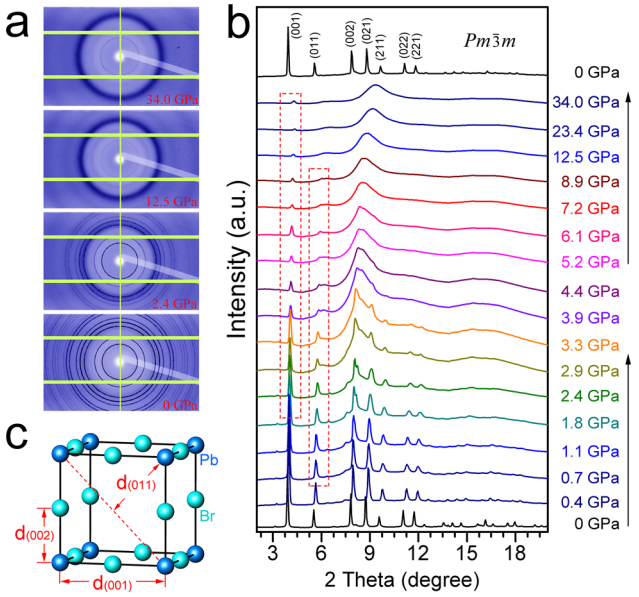

Figure 1. Synchrotron XRD patterns of $MAPbBr_3$ obtained during compression up to 34.0 GPa and decompression: (a) The raw 2D XRD images and (b) integrated 1D XRD profiles. The XRD pattern after decompression can be indexed with the same crystal structure (space group $Pm\bar{3}m$) from the pristine materials. (c) Illustration of the representative interplanar distances in $MAPbBr_3$ lattice (Only Pb and Br atoms are drawn for clarity).

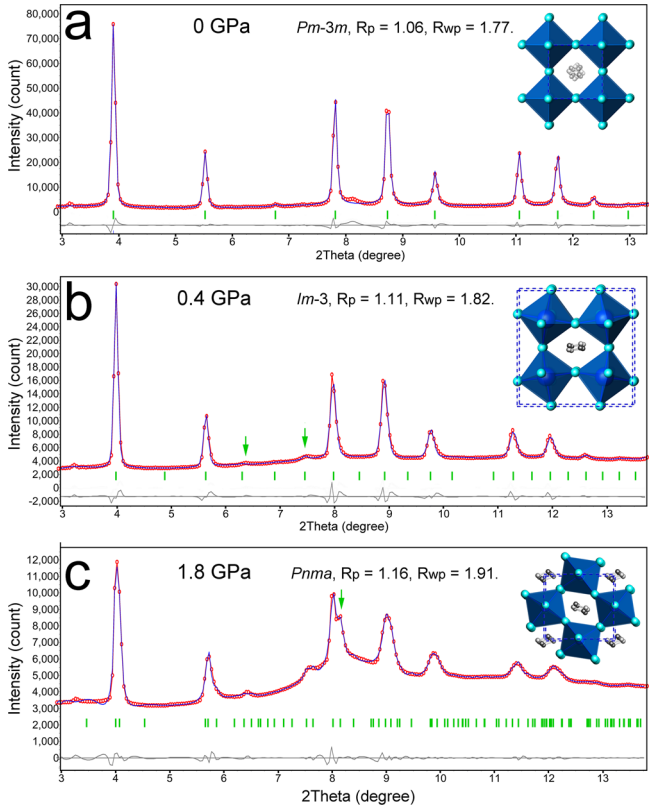

Figure 2. Rietveld refinements of $MAPbBr_3$ under different pressures. (a) Refinement of the ambient XRD data with cubic space group $Pm\bar{3}m$, a = 8.4416(5) Å; (b) Refinement of the 0.4 GPa XRD data with cubic space group $Im\bar{3}$, a = 11.702(5) Å; (c) Refinement of the 1.8 GPa XRD with orthorhombic space group *Pnma*, a = 7.9389(4) Å, b = 11.551(2) Å, c = 8.1544(6) Å). (Experimental: red circle; Simulation: blue line; Bragg reflections: green bar; Deviation: gray line). Inset shows the refined crystal structures of $MAPbBr_3$ with $PbBr_6$ octahedra in blue and C/N atoms in gray.

associated with the amorphous phase. The d value of the strongest broad ring (3.5–4.0 Å) is consistent with the nearest Br–Br distance in close-packed Br^- anions. Figure 1b shows the integrated XRD profiles during compression and recovered to 0 GPa from the highest pressure applied. A subtle structure transformation occurs at very low pressure (0.4 GPa) with the appearance of several small peaks at 6.3, 7.4° (see Figure 2 and subsequent discussions for details). Another phase transformation occurs from 1.8 GPa as evidenced by the obvious splitting of the peak located around 8°. Along with the increasing of applied pressure (above ~2 GPa), broad bands aroused by amorphization dominate the XRD profile. Considering that the crystal structure is built up of inorganic skeleton and organic fillings with different bonding strengths, the pressure-induced amorphization is not surprising. However, some peaks from crystalline $MAPbBr_3$ can remain to relative high pressures. For instance, weak (011) peak is still observable at 8.9 GPa, and (001) can even remain to 34.0 GPa, the highest pressure applied in this study. Note that these peaks are highly related with the long-range ordered packing of heavy atoms Pb and Br (Figure 1c). Thus, the pressure-induced amorphous material should retain the cross-linking $PbBr_6$ perovskite skeleton but with a highly distorted MA molecules. Upon decompression, the amorphous phase returns to the original $MAPbBr_3$ crystalline form and its XRD pattern can be indexed again by using the $Pm\bar{3}m$ unit cell with nearly the same parameters.

At ambient conditions, $CH_3NH_3PbBr_3$ has a cubic space group $Pm\bar{3}m$. There are three phase transitions reported at low temperatures (i.e., to $I4/mcm$ at 236.3 K, to $P4/mmm$ at 154.0 K, and to $Pna2_1$ at 148.8 K),[50] while only one phase transformation from $Pm\bar{3}m$ to $Im\bar{3}$ under high pressure (below 1 GPa) was reported by Swainson et al.[41] They also suggested an orthorhombic phase with space group *Pnma* under higher pressure by DFT calculations. Contractively, in our experiment, we observed the cubic $Im\bar{3}$ structure as an intermediate phase only existed between 0.4 and 1.1 GPa, and starting from 1.8 GPa an orthorhombic *Pnma* structure existed until complete amorphization around 4 GPa. Figure 2 shows the Reitveld refinement profiles for representative XRD data taken at 0, 0.4, and 1.8 GPa. A cubic structure of $MAPbBr_3$ without H atoms was used as starting model for the ambient pattern, and the refinement gave cell parameter: a = 8.4416(5) Å. For the 0.4 GPa pattern, an enlarged cubic unit cell ($Im\bar{3}$, $a = \sqrt{2}a_0$) was adopted to cover the weak emerging peaks (as indicated by the green arrows). While above 1.8 GPa, an orthorhombic unit cell with space group *Pnma* was used to fit the further split diffraction peaks (a = 7.9389(4) Å, b = 11.551(2) Å, c = 8.1544(6) Å). It appears that the tilting distortion of $PbBr_6$ octahedral dominates the two phase transformations ($a^+a^+a^+$ for $Im\bar{3}$, $a^+b^-b^-$ for *Pnma*),[41] and the MA cations may not undergo long-range orientation ordering and only contribute to the broad diffraction background. The phase diagram and cell parameters evolution of $MAPbBr_3$ as a function of pressure are displayed in Figure 3. The two discontinuous phase transformations during compression are marked by the considerable changes in both cell parameters (a, b, c) and cell volumes (V). These phases are termed as phase I ($Pm\bar{3}m$, ambient pressure), phase II ($Im\bar{3}$, 0.4–1.1 GPa) and

DOI: 10.1021/jacs.5b06346
J. Am. Chem. Soc. 2015, 137, 11144–11149

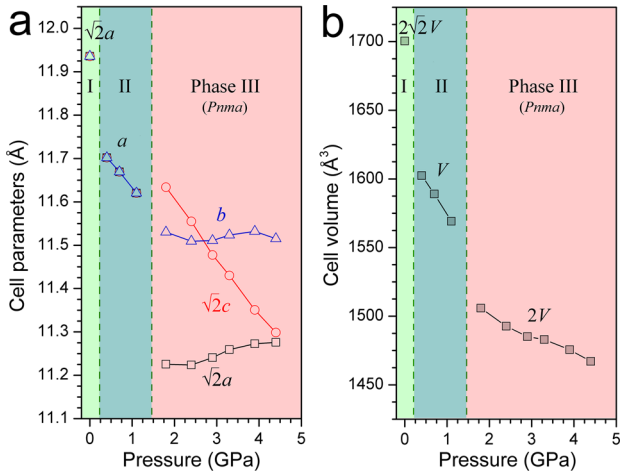

Figure 3. Unit cell parameters (a) and volume evolutions (b) of $MAPbBr_3$ as a function of pressure at room temperature. Space group of I: cubic, $Pm\bar{3}m$; II: cubic, $Im\bar{3}$; III: orthorhombic, *Pnma*.

phase III (*Pnma*, above 1.8 GPa). And the orthorhombic $MAPbBr_3$ shows an anisotropic compressibility because of the different influence of dumbbell-shape MA molecules on the in-phase and out-of-phase titling of $PbBr_6$ octahedra.

One may concern mostly on the pressure effect on the photovoltaic related properties of $MAPbBr_3$, and wonder if high pressure techniques at several GPa level can find application in photovoltaic devices. First of all, we evaluate the band gap evolution by measuring the in situ PL spectra of $MAPbBr_3$ as a function of pressure up to 20.7 GPa. The sample was loaded within a 500 μm culet DAC, irradiated by a 3 mW laser at 325 nm, and the data were taken by using a micro-Raman system. Figure 4 shows the stacked PL curves for $MAPbBr_3$ upon compression and decompression. The ambient sample exhibits a green emission centered at 525 nm corresponding to the near-edge band gap emitting, which is consistent with previous literature.[51] An anomalous peak shift was observed upon

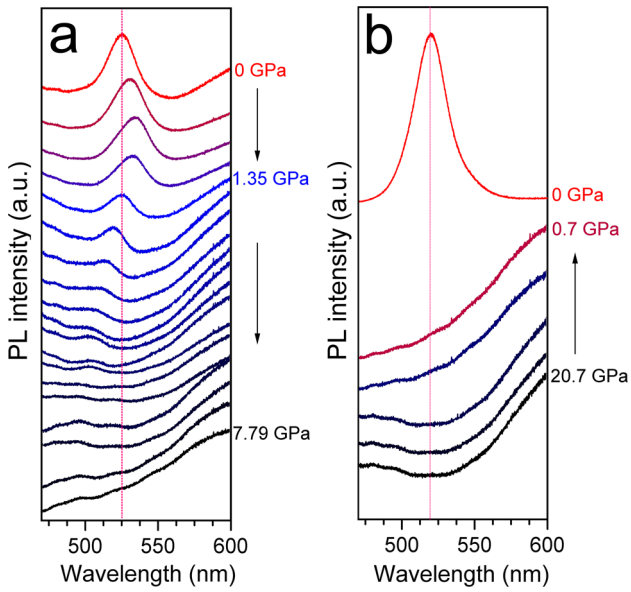

Figure 4. Room temperature photoluminescence spectra of $MAPbBr_3$ as a function of pressure during compression (a) and decompression (b). A 325 nm and 3 mW laser was used for irradiation.

compression: first a gradual red shift in the 0−1 GPa region and followed by a blue shift above 1 GPa. This phenomenon has never been observed before in a crystalline semiconductor because the pressure effect on the electronic structure is usually unidirectional and phase transformations often cause sudden changes of properties. In this case, the abnormal PL/band gap evolutions are attributed to the competition of two forces, compression effect to shorten the bonding length and pressure-induced amorphization to break certain bonds. With increasing pressure, the PL becomes weaker and finally undetectable due to the enhanced nonradioactive processes in the amorphous lattice. Upon pressure releasing, the amorphous $MAPbBr_3$ can regain the green emission located at 520.5 nm, a slight blue-shift compared with the starting material, and restore the ambient crystalline structure.

Figure 5a shows the band gap evolution of $MAPbBr_3$ as derived from PL data. The band gap change value +0.2 eV from

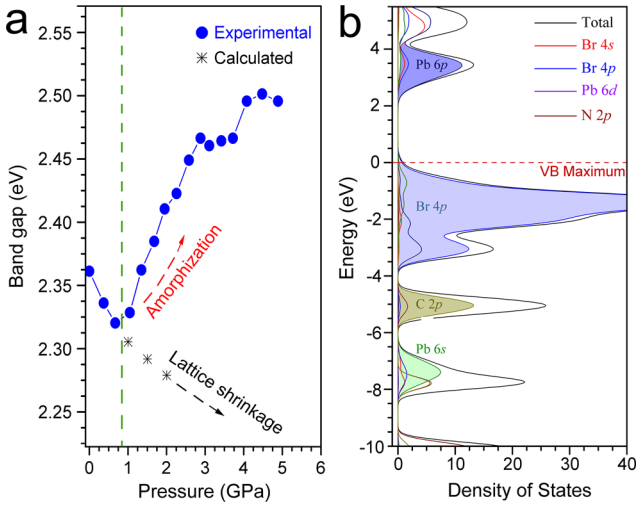

Figure 5. Derived band-gaps of $MAPbBr_3$ as a function of pressure (a) and calculated partial density of states from each element in the compound (b).

1 to 5 GPa, is quite an innegligible effect indicating the potential use of hydrostatic pressure as a control tool in photovoltaic applications. To gain further insight into the anomalous PL behavior of $MAPbBr_3$, first-principles calculations were carried out on both the partial density of states (PDOS) and the evolution of band-gaps under pressure. The results based on orthorhombic $MAPbBr_3$ (*Pnma*) shows that hydrostatic pressure favors to narrow the band gap (red shift to longer wavelength). The observed blue shift in band gap can only be contributed by the pressure-induced amorphization, during which the successive overlap of elemental orbital is suppressed by the breaking of long-range orders. Figure 5b shows the partial contributions of each element to the total density of state. It is clear that the Br 4*p* orbital and Pb 6*p* orbital contribute mostly to the valence band (VB) and conducting band (CB) of $MAPbBr_3$, respectively.[52] So the band gap narrowing upon compression is mainly due to the shrinkage of $PbBr_6$ octahedra and organic MA cations do not contribute on the band gap directly.

The electrical conductivity and photocurrent are important characteristics for a semiconductor with practical applications. To explore the conductivity evolution during the pressure-induced amorphization process, we carried out in situ resistance

DOI: 10.1021/jacs.5b06346
J. Am. Chem. Soc. 2015, 137, 11144−11149

measurement using four-point-probe and quasi-four-point-probe methods within DAC devices (denoted as Cell 1 and Cell 2, see Supporting Information for details). Figure 6a shows

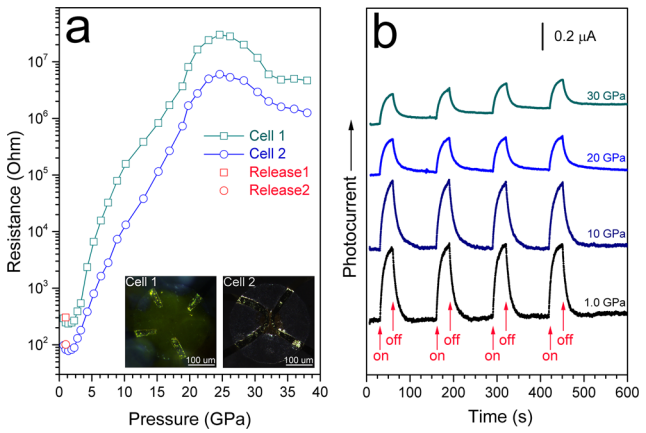

Figure 6. Electrical resistance (a) and photocurrent (b) of $MAPbBr_3$ as a function of pressure. The insert in panel (a) displays microphotographs of the samples in two DACs with Au probes.

the electrical resistance change of $MAPbBr_3$ as a function of pressure upon compression and decompression. In the low pressure region (<2 GPa), no obvious ER changes associated with the above-mentioned two phase transitions are observed. As the applied pressure increases above 2 GPa, both the two samples with different connection configurations show gradually and rapidly increased resistance until reach a plateau around 25 GPa. The maximum resistance reaches 5 orders of magnitude higher than the starting value. Normally, pressure makes atomic distances closer in inorganic semiconductors, which in term the materials performs a better electrical conductivity and even metallization. Here, for $MAPbBr_3$, the increased resistance can be attributed to the pressure-induced amorphization. The phenomenon, giant electrical conductivity change with applied pressure in an optoelectronic material, may provide us some novel applications in photovoltaic devices as switcher or controller.

We also measured the in situ photocurrent of $MAPbBr_3$ under high pressure by using Cell 2. The results are shown in Figure 6b. The material shows obvious response with the on−off switch of the visible light during the entire measured pressure range. Despite the decrease in a certain degree under higher pressure, amorphous $MAPbBr_3$ also exhibits considerable photocurrent up to 30 GPa and even higher pressures, indicating its semiconductor feature. As discussed above, the pressure-induced amorphous $MAPbBr_3$ is a highly ordered glass, or in another word highly disordered crystalline, inheriting the structure feature of the perovskite skeleton as we can recover it back to pristine crystalline phase upon decompression. If such an amorphous $MAPbBr_3$ can be used as photovoltaic materials, what about other amorphous organometal halides synthesized by ambient-pressure methods? The future exploration toward more amorphous organometal salts with comparable or even better performance than their crystalline form may greatly drive the development of perovskite-sensitized solar cells.

CONCLUSION

In conclusion, we studied the structural and visible light response of the organolead halide perovskite, $MAPbBr_3$, as a function of pressure up to 34 GPa at room temperature. Two phase transformations and a reversible amorphization were observed, which could be attributed to the tilting of $PbBr_6$ octahedra and the destroying of long-range ordering of MA molecules, respectively. The visible light responses of $MAPbBr_3$ to pressure, including the band gap shifts, electrical resistance and photocurrent, were studied by in situ high pressure measurements and first-principle simulations. The results show that hydrostatic pressure can greatly affect the crystal structure of organolead halides and their photovoltaic related properties. This demonstration not only provides a possibility of organohalide perovskites applied in photovoltaic devices as switcher or controller, but also sheds light on the exploration of more amorphous organometal composites as potential light absorber.

ASSOCIATED CONTENT

Supporting Information

The Supporting Information is available free of charge on the ACS Publications website at DOI: 10.1021/jacs.5b06346.

Ambient XRD pattern and PL spectra of $MAPbBr_3$; Description of the resistance measurements. (PDF)

AUTHOR INFORMATION

Corresponding Authors

*yyggwang@gmail.com
*yangwg@hpstar.ac.cn
*yusheng.zhao@unlv.edu

Notes

The authors declare no competing financial interest.

ACKNOWLEDGMENTS

The UNLV High Pressure Science and Engineering Center (HiPSEC) is a DOE−NNSA Center of Excellence supported by Cooperative Agreement DE-NA0001982. This research was supported by DOE-BES X-ray Scattering Core Program under Grant Number DE-FG02-99ER45775. HPCAT operations are supported by DOE-NNSA under Award No. DE-NA0001974 and DOE-BES under Award No. DE-FG02-99ER45775, with partial instrumentation funding by NSF. The gas loading was performed at GeoSoilEnviroCARS, APS, ANL, supported by EAR-1128799 and DE-FG02-94ER14466. APS is supported by DOE-BES, under Contract No. DE-AC02-06CH11357. Y. W. also thanks the supporting from National Natural Science Foundation of China (21301063).

REFERENCES

(1) Lee, M. M.; Teuscher, J.; Miyasaka, T.; Murakami, T. N.; Snaith, H. J. *Science* **2012**, *338*, 643−647.
(2) Green, M. A.; Ho-Baillie, A.; Snaith, H. J. *Nat. Photonics* **2014**, *8*, 506−514.
(3) Burschka, J.; Pellet, N.; Moon, S.-J.; Humphry-Baker, R.; Gao, P.; Nazeeruddin, M. K.; Grätzel, M. *Nature* **2013**, *499*, 316−319.
(4) Lotsch, B. V. *Angew. Chem., Int. Ed.* **2014**, *53*, 635−637.
(5) Hodes, G. *Science* **2013**, *342*, 317−318.
(6) Jung, H. S.; Park, N.-G. *Small* **2015**, *11*, 10−25.
(7) Kazim, S.; Nazeeruddin, M. K.; Grätzel, M.; Ahmad, S. *Angew. Chem., Int. Ed.* **2014**, *53*, 2812−2824.
(8) Yang, Z.; Zhang, W.-H. *Chin. J. Catal.* **2014**, *35*, 983−988.
(9) Gao, P.; Grätzel, M.; Nazeeruddin, M. K. *Energy Environ. Sci.* **2014**, *7*, 2448−2463.
(10) Lee, M. M.; Teuscher, J.; Miyasaka, T.; Murakami, T. N.; Snaith, H. J. *Science* **2012**, *338*, 643−647.

DOI: 10.1021/jacs.5b06346
J. Am. Chem. Soc. 2015, 137, 11144−11149

(11) Kim, H.-S.; Lee, C.-R.; Im, J.-H.; Lee, K.-B.; Moehl, T.; Marchioro, A.; Moon, S.-J.; Baker, R. H.; Yum, J.-H.; Moser, J. E.; Grätzel, M.; Park, N.-G. *Sci. Rep.* **2012**, *2*, 591.
(12) Heo, J. H.; Im, S. H.; Noh, J. H.; Mandal, T. N.; Lim, C. S.; Chang, J. A.; Lee, Y. H.; Kim, H. J.; Sarkar, A.; Nazeeruddin, M. K. *Nat. Photonics* **2013**, *7*, 486−491.
(13) Noh, J. H.; Im, S. H.; Heo, J. H.; Mandal, T. N.; Seok, S. I. *Nano Lett.* **2013**, *13*, 1764−1769.
(14) Stoumpos, C. C.; Malliakas, C. D.; Kanatzidis, M. G. *Inorg. Chem.* **2013**, *52*, 9019−9038.
(15) Green, M. A.; Emery, K.; Hishikawa, Y.; Warta, W.; Dunlop, E. D. *Prog. Photovoltaics* **2014**, *22*, 1−9.
(16) Liu, M.; Johnston, M. B.; Snaith, H. J. *Nature* **2013**, *501*, 395−398.
(17) Zhou, H.; Chen, Q.; Li, G.; Luo, S.; Song, T.-B.; Duan, H.-S.; Hong, Z.; You, J.; Liu, Y.; Yang, Y. *Science* **2014**, *345*, 542.
(18) Nagane, S.; Bansode, U.; Game, O.; Chhatre, S.; Ogale, S. *Chem. Commun.* **2014**, *50*, 9741−9744.
(19) Ogomi, Y.; Morita, A.; Tsukamoto, S.; Saitho, T.; Fujikawa, N.; Shen, Q.; Toyoda, T.; Yoshino, K.; Pandey, S. S.; Ma, T.; Hayase, S. *J. Phys. Chem. Lett.* **2014**, *5*, 1004−1011.
(20) Xing, G.; Mathews, N.; Lim, S. S.; Yantara, N.; Liu, X.; Sabba, D.; Grätzel, M.; Mhaisalkar, S.; Sum, T. C. *Nat. Mater.* **2014**, *13*, 476−480.
(21) Navas, J.; Sánchez-Coronilla, A.; Gallardo, J. J.; Hernández, N. C.; Piñero, J. C.; Alcántara, R.; Fernández-Lorenzo, C.; De los Santos, D. M.; Aguilar, T.; Martín-Calleja, J. *Nanoscale* **2015**, *7*, 6216−6229.
(22) Zhang, W.; Anaya, M.; Lozano, G.; Calvo, M. E.; Johnston, M. B.; Míguez, H.; Snaith, H. J. *Nano Lett.* **2015**, *15*, 1698−1702.
(23) Butler, K. T.; Frost, J. M.; Walsh, A. *Mater. Horiz.* **2015**, *2*, 228−231.
(24) Lindblad, R.; Jena, N. K.; Philippe, B.; Oscarsson, J.; Bi, D.; Lindblad, A.; Mandal, S.; Pal, B.; Sarma, D. D.; Karis, O.; Siegbahn, H.; Johansson, E. M. J.; Odelius, M.; Rensmo, H. *J. Phys. Chem. C* **2015**, *119*, 1818−1825.
(25) Jeon, N. J.; Noh, J. H.; Yang, W. S.; Kim, Y. C.; Ryu, S.; Seo, J.; Seok, S. I. *Nature* **2015**, *517*, 476−480.
(26) Zhang, T.; Yang, M.; Benson, E. E.; Li, Z.; Lagemaat, J. V. D.; Luther, J. M.; Yan, Y.; Zhu, K.; Zhao, Y. *Chem. Commun.* **2015**, *51*, 7820−7823.
(27) Mosconi, E.; Umari, P.; Angelis, F. D. *J. Mater. Chem. A* **2015**, *3*, 9208−9215.
(28) Maughan, A. E.; Kurzman, J. A.; Neilson, J. R. *Inorg. Chem.* **2015**, *54*, 370−378.
(29) Yu, H.; Wang, F.; Xie, F.; Li, W.; Chen, J.; Zhao, N. *Adv. Funct. Mater.* **2014**, *24*, 7102−7108.
(30) Filip, M. R.; Eperon, G. E.; Snaith, H. J.; Giustino, F. *Nat. Commun.* **2014**, *5*, 5757.
(31) Eperon, G. E.; Stranks, S. D.; Menelaou, C.; Johnston, M. B.; Herz, L. M.; Snaith, H. J. *Energy Environ. Sci.* **2014**, *7*, 982−988.
(32) Hao, F.; Stoumpos, C. C.; Cao, D. H.; Chang, R. P. H.; Kanatzidis, M. G. *Nat. Photonics* **2014**, *8*, 489−494.
(33) Pellet, N.; Gao, P.; Gregori, G.; Yang, T.-Y.; Nazeeruddin, M. K.; Maier, J.; Grätzel. *Angew. Chem., Int. Ed.* **2014**, *53*, 3151−3157.
(34) Jaffe, A.; Lin, Y.; Mao, W. L.; Karunadasa, H. I. *J. Am. Chem. Soc.* **2015**, *137*, 1673−1678.
(35) Mao, W. L.; Wang, L.; Ding, Y.; Yang, W.; Liu, W.; Kim, D.; Luo, W.; Ahuja, R.; Meng, Y.; Sinogeikin, S.; Shu, J.; Mao, H.-K. *Proc. Natl. Acad. Sci. U. S. A.* **2010**, *107*, 9965−9968.
(36) Ma, Y.; Eremets, M.; Oganov, A. R.; Xie, Y.; Trojan, I.; Medvedev, S.; Lyakhov, A. O.; Valle, M.; Prakapenka, V. *Nature* **2009**, *458*, 182−185.
(37) Wang, L.; Liu, B.; Li, H.; Yang, W.; Ding, Y.; Sinogeikin, S. V.; Meng, Y.; Liu, Z.; Zeng, X. C.; Mao, W. L. *Science* **2012**, *337*, 825−828.
(38) Yao, M.; Wang, T.; Yao, Z.; Duan, D.; Chen, S.; Liu, Z.; Liu, R.; Lu, S.; Yuan, Y.; Zou, B.; Cui, T.; Liu, B. *J. Phys. Chem. C* **2013**, *117*, 25052−25058.
(39) Zhang, M.; Dang, Y.; Li, H.-W.; Wu, Y.; Li, Q.; Wang, K.; Zou, B. *J. Phys. Chem. C* **2013**, *117*, 639−647.
(40) Li, Q.; Li, S.; Wang, K.; Li, W.; Liu, J.; Liu, B.; Zou, G.; Zou, B. *J. Chem. Phys.* **2012**, *137*, 184905.
(41) Swainson, I. P.; Tucker, M. G.; Wilson, D. J.; Winkler, B.; Milman, V. *Chem. Mater.* **2007**, *19*, 2401−2405.
(42) Gesi, K. *Ferroelectrics* **1997**, *203*, 249−268.
(43) Onoda-Yamamuro, N.; Matsuo, T.; Suga, H. *J. Phys. Chem. Solids* **1990**, *51* (12), 1383−1395.
(44) Mao, H. K.; Xu, J.; Bell, P. M. *J. Geophys. Res.* **1986**, *91*, 4673−4676.
(45) Hammersley, A. P.; Svensson, S. O.; Hanfland, M.; Fitch, A. N.; Häusermann, D. *High Pressure Res.* **1996**, *14*, 235−248.
(46) Rodriguez-Carvajal, J. *Phys. B* **1993**, *192*, 55−69.
(47) Clark, S. J.; Segll, M. D.; Pickard, C. J.; Hasnip, P. J.; Probert, M. I. J.; Refson, K.; Payne, M. C. *Z. Kristallogr.* **2005**, *220*, 567−570.
(48) Ceperley, D. M.; Alder, B. J. *Phys. Rev. Lett.* **1980**, *45*, 566.
(49) Pfrommer, B. G.; Cote, M.; Louie, S. G.; Cohen, M. L. *J. Comput. Phys.* **1997**, *131*, 233−240.
(50) Onoda-Yamanuro, N.; Yamamuro, O.; Matsuo, T.; Suga, H. *J. Phys. Chem. Solids* **1992**, *53*, 277−281.
(51) Schmidt, L. C.; Pertegás, A.; González-Carrero, S.; Malinkiewicz, O.; Agouram, S.; Espallargas, G. M.; Bolink, H. J.; Galian, R. E.; Pérez-Prieto, J. *J. Am. Chem. Soc.* **2014**, *136*, 850−853.
(52) Wang, Y.; Sumpter, B. G.; Huang, J.; Zhang, H.; Liu, P.; Yang, H.; Zhao, H. *J. Phys. Chem. C* **2015**, *119*, 1136−1145.

DOI: 10.1021/jacs.5b06346
J. Am. Chem. Soc. 2015, 137, 11144−11149